

The microstructure and He⁺ ion irradiation behavior of novel low-activation W-Ta-Cr-V refractory high entropy alloy for nuclear applications



D. Kalita ^{a,*}, I. Józwik ^a, Ł. Kurpaska ^a, Y. Zhang ^{b,c}, K. Mulewska ^a, W. Chrominski ^{a,d}, J. O'Connell ^e, Y. Ge ^f, W.L. Boldman ^c, P.D. Rack ^c, Y. Wang ^g, W.J. Weber ^c, J. Jagielski ^{h,i}

^a NOMATEN Centre of Excellence, National Centre for Nuclear Research, A. Soltana 7 St., 05-400 Otwock, Poland

^b Condensed Matter Physics, Energy and Environment Science & Technology, Idaho National Laboratory, Idaho Falls, ID 83415, USA

^c Department of Materials Science & Engineering, University of Tennessee, Knoxville, TN 37996, USA

^d Warsaw University of Technology, Faculty of Materials Science and Engineering, Wołoska 141 St., 02-507 Warsaw, Poland

^e Centre for HRTEM, Nelson Mandela University, Port Elizabeth 6031, South Africa

^f VTT Technical Research Centre of Finland, Ltd., Finland

^g Materials Science and Technology Division, Los Alamos National Laboratory, Los Alamos, NM, USA

^h National Centre for Nuclear Research, A. Soltana 7 St., 05-400 Otwock, Poland

ⁱ Lukasiewicz Research Network – Institute of Microelectronics and Photonics, Al. Lotników 32/46, Warsaw, Poland

ARTICLE INFO

Keywords:

High-entropy alloys
HEA
Ion irradiation
He bubbles
Radiation damage
He irradiation

ABSTRACT

Microstructure and nanohardness of a nearly equimolar W-Ta-Cr-V high entropy alloy (HEA), as well as its irradiation response under He⁺ irradiation, were investigated. The single-phase body-centered cubic nanostructured alloy with a 1 μm thick layer was fabricated on a silicon substrate using a magnetron sputtering method. The HEA film has a complex microstructure consisting of micrometric domains that exhibit internal nanostructure controlled by their crystal orientation. The measured nanohardness of the W-Ta-Cr-V alloy is 13 ± 2 GPa, which significantly exceeds the hardness of nanocrystalline tungsten as a result of the high solid-solution strengthening effect. In order to evaluate the irradiation resistance of the HEA film, the material was irradiated with 200 keV He⁺ ions at room temperature, with two different ion fluences: 1 × 10¹⁶ and 5 × 10¹⁶ ions/cm². Using transmission electron microscopy, a high density of extremely fine He bubbles is observed that were uniformly distributed in the matrix. The increase of He⁺ ion fluence increased the density of bubbles, whereas their size remained at a similar level, which indicates that the damage proceeds by the nucleation of additional He bubbles, not by their growth.

Introduction

The most crucial components of fusion reactors, such as divertor and plasma-facing materials (PFMs), are exposed to unprecedented conditions, i.e. elevated temperatures (>1000 K), large heat loads (10–20 MW/m²), irradiation by the high-energy neutrons (14.1 MeV) and particles such as hydrogen isotopes (D, T) and helium (fluxes > 10²³ m⁻²s⁻¹) [1]. Tungsten is the most important candidate for this application because of its high thermal stability, limited sputtering yield and low tritium uptake. Because of these superior properties, pure tungsten has been applied as the PFM in the International Thermonuclear Experimental Reactor (ITER) [2]. Despite the aforementioned

advantages, the weakness of the tungsten arises from the low fracture toughness, radiation-induced embrittlement and unsatisfactory resistance to damage induced by the high fluxes of low energy particles originating from the plasma [3,4]. Several different effects have been observed when tungsten is subjected to low-energy irradiation by He⁺ ions, including blistering, fuzz microstructure, formation of He bubbles and voids [3,5,6]. These concerns force the search for new materials capable of working in the harsh environment of fusion reactors.

Recently, high entropy alloys (HEAs), also known as concentrated solid-solution alloys (CSAs), are gaining significant attention in the nuclear materials field. These alloys are defined as materials containing multiple principal alloying elements in equimolar or near equimolar

* Corresponding author.

E-mail address: Damian.Kalita@ncbj.gov.pl (D. Kalita).

ratios or at high concentrations [7,8]. As pointed out in several recent reviews, these materials tend to form simple solid-solution systems, such as face-centered cubic (FCC) or body-centered cubic (BCC) [8,9]. The random distribution of differently-sized atoms in the crystal structure of HEAs creates severe chemical disorder that induces noticeable lattice distortions, especially in some BCC alloys [8]. However, the recent works have shown that the chemical disorder does not monotonically raise with the number of alloying elements, as its level depends greatly on the characteristics of the specific elements [10]. The severe lattice distortions can macroscopically result in the intense strengthening of these materials. Because of that, some of the HEAs exhibit exceptional mechanical properties compared to conventional alloys, including high hardness, high yield strength, good ductility, and excellent fracture toughness. Considering the application of HEAs as PFM, some of the most critical issues are high thermal stability and irradiation resistance. These requirements are met by alloys containing mainly refractory metals (Nb, Ta, Mo, W, Re) consequently called refractory high entropy alloys (RHEAs) [13]. RHEAs typically crystallize in a single BCC structure and demonstrate excellent mechanical properties at elevated temperatures [11]. For example, equimolar Nb-Mo-Ta-W alloy fabricated by Senkov et al. [14] exhibits yield strength (YS) of about 400 MPa at the temperature of 1600 °C. Initially, RHEAs were based only on refractory elements, but subsequently, other non-refractory metals, such as Ti, Hf, V or Cr were used to enhance further their performance [15].

In contrast to W and W-based alloys, the irradiation resistance of HEAs has not been well studied yet. Several studies showed that selected HEAs, mainly with the FCC structure, exhibited good phase stability under the irradiation, e.g., Al-Co-Cr-Fe-Ni [16], Fe-Cr-Co-Ni [17] or Co-Cr-Cu-Fe-Ni [18]. However, it is commonly known that FCC alloys are more vulnerable to void swelling than materials with the BCC structure [19]. Therefore, they are generally not considered in the PFM design process. Furthermore, to reduce the amount of long-lived radioactive isotopes formed in transmutation reactions, using only low-activation elements such as Ti, Cr, V, Ta, or W is required [20]. These limitations significantly narrow the number of possible alloy compositions capable of enduring the severe fusion reactor environment. Sadeghilaridjani et al. [21] compared the irradiation behavior of reduced activation BCC Hf-Ta-Ti-V-Zr HEA with 304 stainless steel. They found that under the same irradiation condition (~30 dpa), the hardening of Hf-Ta-Ti-V-Zr alloy is significantly reduced. Similarly, Chang et al. [22] showed that the swelling and hardening effects in BCC Hf-Nb-Ta-Ti-Zr HEA were significantly suppressed up to 30 dpa compared to the conventional nuclear materials. Very recently, El-Atwani et al. [23] fabricated low-activation W38-Ta36-Cr15-V11 (in at.%) HEA with the BCC crystalline structure using a magnetron sputtering method. Surprisingly, the material showed no sign of irradiation-induced structural defects and negligible irradiation hardening up to 8 dpa. Although underlying mechanisms remain unclear, presumably, it is connected with the high chemical complexity of these materials leading to local structural distortions [24]. Considering the atomic scale, the variable local elemental environment results in variations in the formation and migration energies of defects, the presence of local traps, and the existence of anisotropic diffusion channels [8]. These affect defects' evolution by reducing their mobility and increasing their recombination rate [8,25]. Taking this into consideration, the enhanced irradiation-resistance of the HEAs is most likely related to the increased vacancy-interstitial recombination rate in comparison to pure metals and traditional alloys [26,27]. This is quite different from the behavior of W, in which the significant variations in defects mobility resulted in the formation of dislocation loops and irradiation hardening effect [28,29].

Although low-activation RHEAs are considered an alternative of W for PFM, the data concerning the impact of He⁺ ion irradiation on the performance of those alloys are limited. El-Atwani et al. [30] studied the behavior of the W35-Ta35-V15-Cr15 alloy under low-energy He⁺ irradiation at a temperature of 1223 K. They observed very small He bubbles (2–3 nm) uniformly distributed in the material's microstructure. They

concluded that the overall He⁺ irradiation resistance of the W35-Ta35-V15-Cr15 alloy is higher compared to pure W due to slow diffusion and accumulation of He during the irradiation. Similarly, Cui et al. [31] reported very high surface stability of sintered W(TaVCrTi)_x (where x = 10, 20, 30, and 40) alloys under He⁺ ion irradiation in comparison to W.

In summary, despite the growing interest in W-Ta-Cr-V-based RHEA and its application in a nuclear environment, the alloy with the equimolar composition, which shows an elevated chemical disorder in comparison to compositions studied to date, has not been investigated so far. The high level of chemical disorder of this material arises from the difference in atomic mass and volume between the period 4 alloying elements (V and Cr) and the period 6 elements (Ta and W) [8]. This is particularly important from the point of view of its resistance to irradiation damage, microstructural changes, and their impact on the mechanical properties, as reported in recent works [25,26,32]. Considering this, the main aim of the presented research was to fabricate a new, equimolar W-Ta-Cr-V alloy and to characterize its resistance against He-induced damage accumulation during He⁺ ion irradiation.

Experimental

Material fabrication

The experimental material was synthesized using a magnetron sputtering method in the form of a 1 μm thick layer on a silicon substrate. Although the technique is not suitable for bulk materials production, it can be successfully used for the relatively straightforward fabrication of new compositions of HEAs for research purposes on the laboratory scale. Taking this into account the difficulties with the preparation of the HEAs in the bulk form, the method may be promising approach for synthesizing new HEAs. This would facilitate the initial assessment of their irradiation resistance and the development of the most promising compositions, which could then be fabricated in bulk form for further study in subsequent steps. The deposition process of the investigated W-Ta-Cr-V alloy was carried out at room temperature (RT) with target power set to at 200 W (445 V) for 2 h 35 min. The AJA International ATC 2400-V magnetron sputtering system was used. The substrate was rotating during the sputtering deposition to obtain a uniform film. The more details concerning the fabrication process can be found in [33].

He⁺ ions irradiation

The RT ion irradiation of the as-deposited samples was carried out with He⁺ ions using a 200 kV Danfysik Research Ion Implanter in the Ion Beam Materials Laboratory at Los Alamos National Laboratory. The samples were mounted on a copper block using double sided carbon tape. A thermocouple was fixed on the block to track the sample's temperature throughout the implantation process. All samples were uniformly implanted with a beam flux of approximately $4.8 \times 10^{12} \text{ cm}^{-2} \text{s}^{-1}$. Two different ion fluences of $1 \times 10^{16} \text{ cm}^{-2}$ and $5 \times 10^{16} \text{ cm}^{-2}$ were achieved, described hereafter as LF (low fluence) and HF (high fluence), respectively. No temperature increase from the beam heating was expected or detected. The process was conducted in the vacuum chamber (pressure below 5×10^{-7} Torr). The damage profiles and helium distribution in irradiated materials, presented in Fig. 1, were calculated using the Stopping and Range of Ions in Matter (SRIM) software in a Full Cascade mode [34]. For complex alloys containing transition metals from different periods, showing the significant differences in atomic mass (e.g., periods 4 and 6 of W-Ta-Cr-V in this study), SRIM predictions of displacements per atom (dpa) depend on the input parameters [35,10]. The displacement energy for the elements of V, Cr, Ta and W were set as 57, 40, 90, and 90 eV, respectively [36]. Theoretical density for the equimolar composition of the alloy of 12.28 g/cm^3 was used. The atomic density of the material of $6.32 \times 10^{22} \text{ cm}^{-3}$, was estimated using SRIM software. According to Fig. 1, the maximum

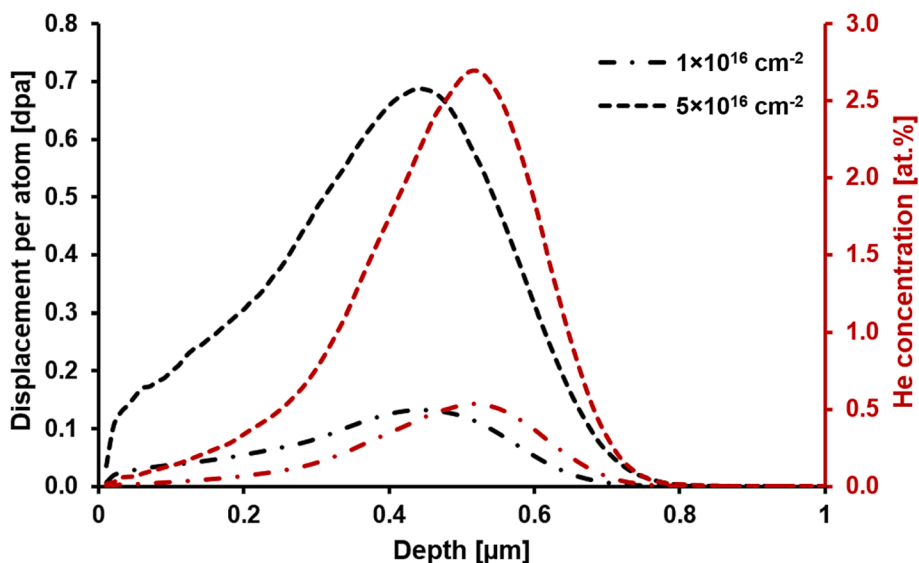


Fig. 1. Damage accumulation (black lines and left axis) and He concentration (red lines and right axis) in W-Ta-Cr-V HEA as a function of the depth calculated using SRIM software.

damage levels of 0.15 dpa (LF) and 0.75 dpa (HF) were observed at a depth of about 450 nm. The He-concentration peak was slightly shifted to about 500 nm, where the concentration of He reached 0.5 at.% and 2.5 at.% for LF and HF samples, respectively.

Materials characterization

The microstructure of the alloy was characterized using a scanning electron microscope (SEM) ThermoFisher Scientific Helios 5 UX. The microscope is equipped with the focused ion beam (FIB), EDAX Octane Elite Plus energy-dispersive X-ray spectroscopy (EDS) system and EDAX Velocity Pro electron backscatter diffraction (EBSD) camera. More detailed microstructural analysis was carried out by transmission electron microscopes (TEM), JEOL JEM 1200EX II operating at 120 kV, ThermoFisher Scientific Talos F200 G2 and JEOL ARM-200F operating at 200 kV, the latter equipped with electron energy loss spectrometer (EELS). Thin foils for the TEM analysis were prepared by FIB lift-out technique. To reduce the effect of the preparation of the microstructure of the samples, the final thinning was carried out using 2 keV Ga⁺ beam. The average thickness of thin foils for TEM observations, measured using the EELS technique, was about 60 nm. The transmission Kikuchi diffraction (TKD) orientation maps were acquired in off-axis geometry using an EDAX Velocity Pro EBSD camera. The samples for TKD measurements were prepared by the FIB lift-out technique. Individual foils were tilted by 20° from horizontal. An electron accelerating voltage of 30 kV and a probe current of 3.2nA were used. The TKD maps were collected with a step size of 5 nm. The obtained data were subsequently analyzed with EDAX OIM Analysis 8 software. The points with the confident index (CI) < 0.1 were removed from the calculations. The results were presented in the form of orientation and Kernel Average Misorientation (KAM) maps. The latter is the representation of a local grain misorientation. KAM calculates the average misorientation around a measurement point concerning its nearest neighbor points [37].

Nanoindentation tests were performed using a NanoTest Vantage system (Micro Materials Ltd.) with a Berkovich-shaped diamond indenter tip. The investigations were performed at RT using single load mode. It is well established that the tip plays a significant role in low load nanoindentation [38]. Before the tests, the diamond area function (DAF) of the indenter was calibrated using fused silica. Measurements were carried out in a single force mode by using various values of loads in the range from 0.25 mN to 10 mN, giving deformation range of approx. 20 nm to 150 nm. For each load 20 tests were carried out.

Mapping was also done to examine the microstructure of the material using load of 4 mN (depth ~ 80 nm) in a 6 × 6 matrix arrangement (36 measurements in total). The distance between the indents was 20 μm. The nanohardness values were extracted from the nanoindentation load–displacement (L-D) curves by implementing Oliver and Pharr method [39].

Results and discussion

Material characterization

The SEM micrographs revealing the typical surface morphology of the investigated material in as-deposited state are presented in Fig. 2. The areas of various microstructure with a size of a few μm showing the “serrated” nanometric crystals and flat regions can be easily distinguished, as follows from Fig. 2(a). The images indicate that the layer is partly comprised of nanometric crystals of similar orientations arranged differently in various regions, which has been verified by TKD results presented in Fig. 5. This characteristic morphology, appearing in the materials obtained by the magnetron sputtering method, is known as domain-grain (or grain-subgrain) structure, where high-angle grain boundaries may be distinguished as domain boundaries [40]. Similar microstructures were observed among others for sputtered tin-doped indium oxide (ITO) [40,41]. The formation of domain-grain structures is commonly attributed to the variations in resputtering ratios among different crystallographic planes exposed at the material’s surface during the deposition [41]. The chemical composition of the fabricated alloy was studied using the EDS technique. The EDS spectra were acquired in five 200 × 200 μm areas, and each element’s average atomic concentration was calculated using existing algorithms in the EDS software. The results of calculations presented in Table 1 indicate that the concentrations of all elements remain at similar level. Taking this into account, the fabricated alloy can be considered equimolar. To investigate the distribution of the elements within the layer, the EDS analysis was also performed also on cross-section of the layer using the STEM technique. Fig. 3 shows the STEM/BF image and the corresponding elemental maps. All elements were uniformly distributed in the layer without any notable segregation.

A more detailed analysis of the layer microstructure has been performed using transmission electron microscopy. Fig. 4 shows the bright field (BF) TEM image showing the microstructure of the as-deposited W-Ta-Cr-V layer. One may distinguish the nano-columns of a width of

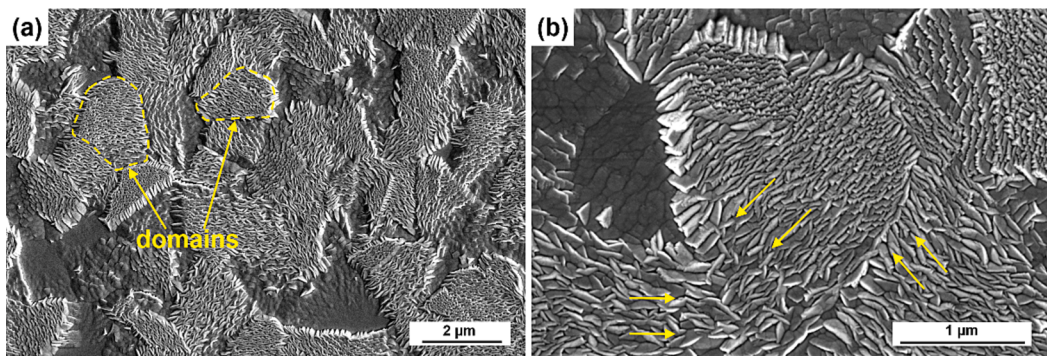


Fig. 2. SEM images of the W-Ta-Cr-V alloy at low (a) and high (b) magnification. The arrows in (b) show the various arrangement of nanocrystals in different domains.

Table 1

Average chemical composition of the as-deposited layer obtained using the EDS technique.

Element	W	Ta	Cr	V
Content [at.%]	26 ± 1	24 ± 1	26 ± 1	24 ± 2

10–50 nm elongated in the layer growth direction. The selected area electron diffraction (SAED) pattern corresponds to the BCC structure, with no extra spots related to any secondary phases. Considering this, it may be concluded that the equimolar W-Ta-Cr-V HEA exhibits a high tendency to form a single-phase solid solution. The presence of solid solutions was already reported for several multicomponent HEAs [8–42]. This included the best-known equimolar FCC-structured Fe-Cr-Mn-Ni-Co Cantor alloy [7] or BCC-structured Ta-Nb-Hf-Zr-Ti HEA [43]. The appearance of single-phase solid solutions in HEAs is simply explained by the enhanced entropy of mixing compared to conventional alloys [44], although entropic stabilization may not be predominant and is a matter for debate [8,45]. Although the equimolar HEAs reach the maximum entropy of mixing, they also frequently form intermetallic compounds or a mixture of solid solutions, e.g., Zr₂Al intermetallic phase in Al-Nb-Ti-Zr [46] or a mixture of disordered BCC and ordered B2 structures in Al-Co-Cr-Fe-Ni [47]. Considering this, the experimental verification of the phase compositions of new HEAs frequently seems to be essential. So far, the experimental data are very limited in the case of alloys based on the studied W-Ta-Cr-V quaternary system. The only materials investigated experimentally, which can be found in the literature, are non-equimolar W38-Ta36-Cr15-V11 and W35-Ta35-V15-Cr15 HEAs developed by El-Atwani et al. [23,30] and W42-Ta-39-V8-Cr11 reported by Shi et al. [48]. All these materials were prepared using

magnetron sputtering and exhibited a single-phase BCC structure. The results obtained in this work indicate that the equimolar W-Ta-Cr-V HEA forms a single-phase BCC solid solution, which may be essential from the point of view of further research on the application of this material in the nuclear industry.

As mentioned, in order to investigate the microstructure of the fabricated W-Ta-Cr-V alloy in more detail, the Transmission Kikuchi Diffraction (TKD) technique was used. Fig. 5(a) shows the topography of the material with two various regions (marked with arrows), which, based on their morphology, were denoted as “serrated” and “flat”. The area containing one “flat” and two “serrated” domains, which has been further used for preparation of cross-sectional micro-lamella for TKD, is marked in the image with a dashed rectangle. The TKD orientation map for this region is presented in Fig. 5(b). It was found that the “serrated” areas are characterized by the internal nano-columnar microstructure, whereas no internal grain refinement was registered in the case of “flat” domains. The specific microstructure of the domains is closely related to their crystal orientation. The “serrated” domains exhibit orientations close to $\langle 011 \rangle$ or $\langle 111 \rangle$ relative to the surface, whereas the “flat” ones are $\langle 001 \rangle$ -oriented. It is also worth noting that, apart from the microstructural differences, the individual regions exhibit various heights (in fact thicknesses of the original deposited HEA layer). In this case, the “serrated” domains are slightly higher in comparison to “flat” ones, as revealed from both SEM observations as well as the TKD map (Fig. 5). Fig. 6 shows the TKD orientation map acquired for the group of two selected “serrated” domains. The careful analysis of the obtained map shows that the domains initially grow in the form of planar grains separated by high-angle grain boundaries (HAGBs) (Fig. 6(a)). However, with increasing distance from the Si substrate the misorientations in the layer increase, as can be seen from the Kernel Average Misorientation

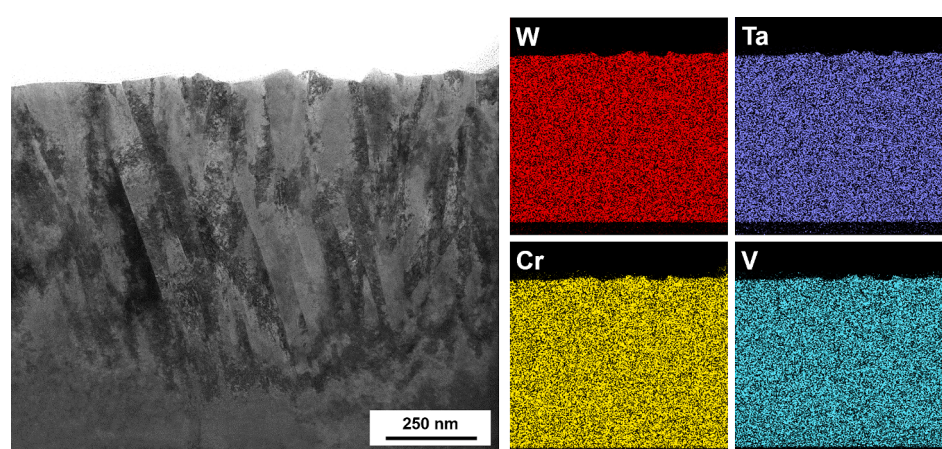


Fig. 3. STEM/BF microstructure of the cross-section of W-Ta-V-Cr layer and corresponding EDS (at.%) elemental maps.

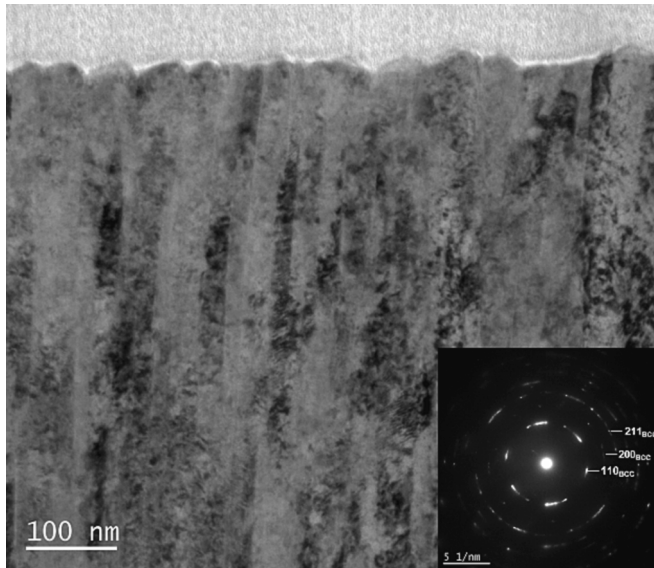


Fig. 4. TEM/BF micrograph and corresponding SAED pattern of the as-deposited W-Ta-Cr-V HEA.

(KAM) map presented in Fig. 6(b). The gradual fragmentation of the initially homogeneous domain into nanometric columns separated mainly by the low-angle grain boundaries (LAGBs) occurs with the increasing thickness of the layer. Each domain contains numerous individual nanocolumns (see Fig. 2 and Fig. 6) that exhibit only slight orientation deviation compared to the initial orientation of the domain. Similar microstructures of sputtered tungsten layers, known as

nanoridges, were previously reported in the literature, e.g. [49,50]. Their origin can be attributed to the anisotropic surface diffusion coefficients along different crystallographic directions. For example, in the study conducted by Singh et al. [50], the presence of nanridge domains in (110)-oriented tungsten was ascribed to the existence of fast diffusion channels along the $\langle 111 \rangle$ directions. However, also other processes such as resputtering, internal stresses, or surface instabilities may affect the formation of nanoridges structure [41,51].

Nanoindentation

Mechanical properties of the investigated W-Ta-Cr-V HEA film in both as-deposited and He^+ -irradiated conditions were evaluated using nanoindentation. Fig. 7 shows the hardness of the layer as a function of depth. Initially, up to about 50 nm contact depth, one can observe that the recorded hardness increases (region I). This is related to the fact that, at low indentation depths, the indenter tip is initially round, causing most of the deformation to arise from the elastic response. Consequently, the mean contact pressure, used as a measure of hardness, does not accurately represent the actual materials properties. This effect is well-documented in the literature [38] and is especially prominent in hard materials. Secondly, it is possible that when probing “serrated” regions composed of nanograins (as pictured in Fig. 5), one is “pushing” fine grains, which leads to their local deformation and rearrangement. Ultimately, this lowers the measured hardness values for small loads. In region II (marked in Fig. 7), the recorded hardness value for the as-deposited material more-or-less stabilizes and reaches a value of 13 ± 2 GPa in the 50–100 nm range. A relatively large deviation of the error bars is related to the “serrated” surface morphology of the layer since the actual measurement is strongly correlated with the microstructure of the tested region. Similar hardness values were already reported for the magnetron sputtered, non-equimolar W38-Ta36-Cr15-V11 HEA [23].

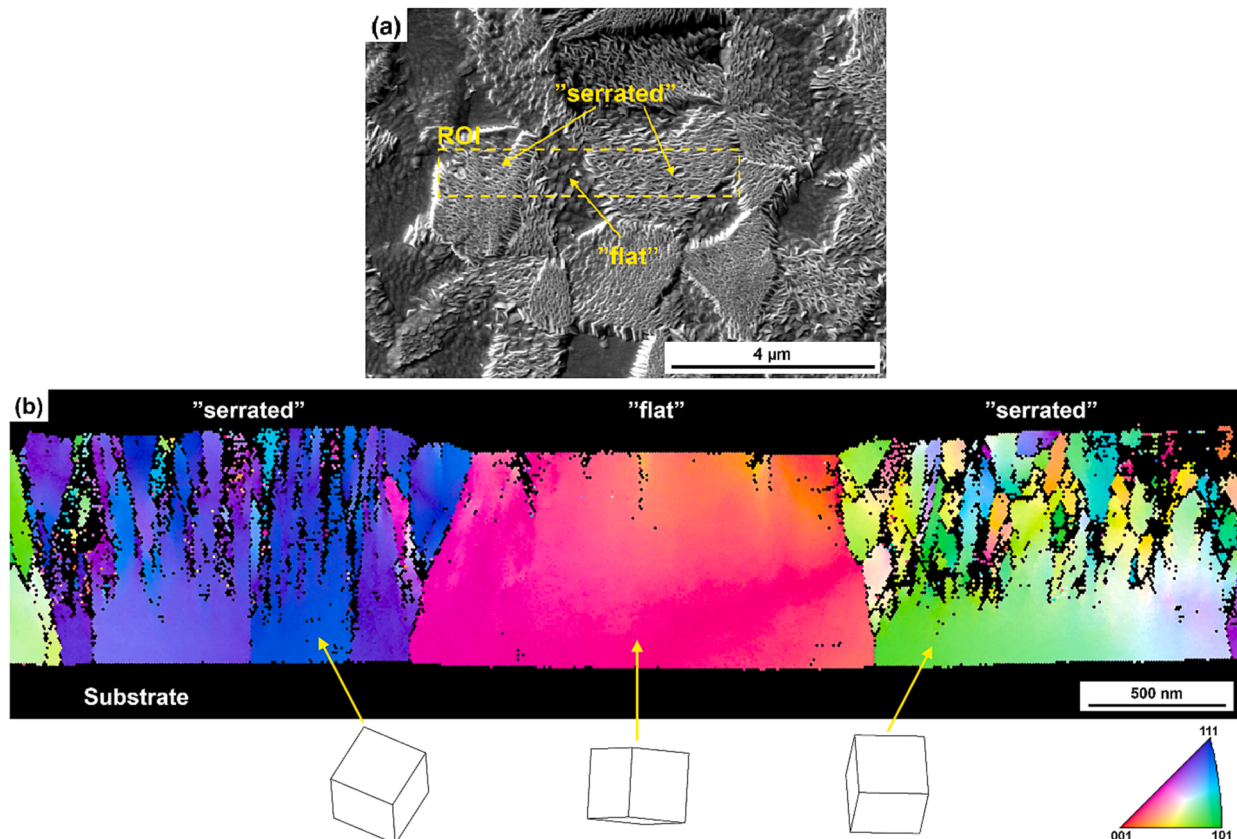


Fig. 5. The SEM topography image of the studied material, with the marked place (ROI) of FIB lamella extraction (a) and TKD orientation map (coloring in the reference of surface) acquired from the cross-section of this region (b).

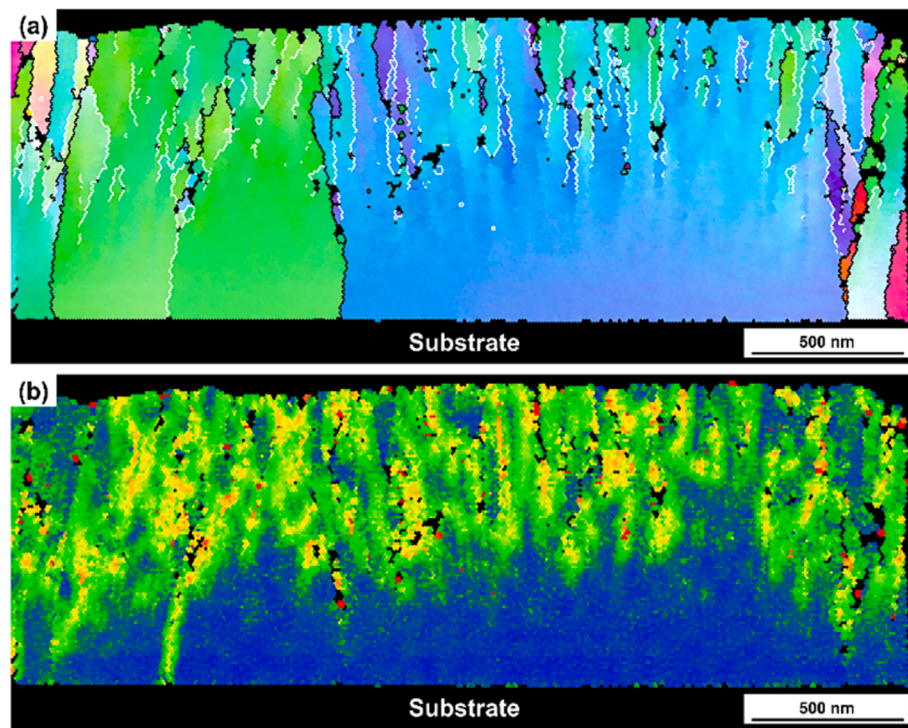


Fig. 6. TKD orientation (a) and KAM maps (b) for the “serrated” region of the W-Ta-V-Cr HEA layer. The low and high-angle grain boundaries on the TKD map are indicated in (a) by white and black lines, respectively.

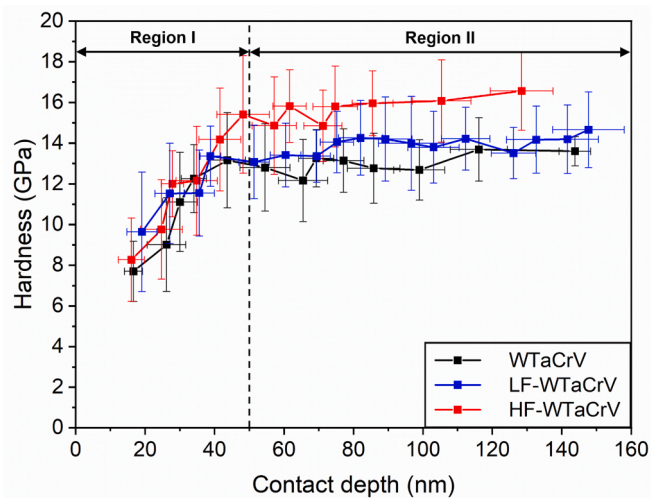


Fig. 7. Hardness as a function of contact depth obtained using nanoindentation technique for as-deposited and He⁺-ion irradiated W-Ta-Cr-V alloy.

On the other hand, lower hardness levels of 9 GPa and 8 GPa were observed for the nanocrystalline and coarse-grained pure W, respectively [52]. Even severely plastically deformed by high-pressure torsion (HPT), pure W demonstrated a lower nanohardness of 11 GPa [53]. The high hardness of the fabricated material in this work results from its fine microstructure, as well as from the solid-solution strengthening effect. Solid-solution strengthening is one of the most crucial strengthening mechanism responsible for the exceptional mechanical properties of HEAs [12]. The introduction of multiple substitutional elements into the random solid-solution structure causes lattice distortion [12]. In the case of the investigated material here, the elements employed show considerable differences in atomic volumes, i.e., W – 16.1, Ta – 18.3, Cr – 11.6 and V – 13.2 Å³ [8]. Because of that, they create significant strains in the

crystal structure. The stress fields introduced by the substitutional atoms impede dislocation motions in the structure of this material during the plastic deformation, which increases its hardness.

As is evident from Fig. 7, the hardness of the investigated material slightly increases after He⁺-irradiation, however, these changes mainly fall within the measurement error. The calculated nanohardness for indentation depths in the range of 50–100 nm increases from the initial 13 ± 2 GPa for the pristine material to 14 ± 2 GPa and 15 ± 2 GPa for the samples irradiated with fluences of 1×10^{16} cm⁻² and 5×10^{16} cm⁻², respectively. This small but progressive enhancement in nanohardness suggests that He⁺-irradiation may induce localized strengthening effects within the W-Ta-Cr-V HEA film, potentially owing to radiation-induced defects or other microstructural changes. Previous studies indicate that defects, such as dislocation loops or He bubbles, formed within the structures of various metallic materials during He⁺-irradiation, act as barriers to dislocation movement, resulting in significant irradiation-hardening [54]. This phenomenon was previously observed among others for pure W, for which the increase of the nanohardness from about 6.5 GPa to 10.5 GPa (in the hardness peak area) after the He⁺-irradiation at RT (fluence 10^{17} cm⁻²) was reported [55]. Similarly, an increase in nanohardness after RT He⁺-irradiation has been found in various HEAs, such as Al_{1.5}CoCrFeNi [56]. However, in this case, the observed changes in nanohardness following the He⁺-irradiation are significantly reduced. This is in a good agreement with the findings of El-Atwani et al. [23], which demonstrate negligible irradiation-hardening of the non-equimolar W₃₈Ta₃₆Cr₁₅V₁₁ HEA during the heavy-ion irradiation up to 8 dpa.

The high standard deviations of the obtained results are related to the characteristic microstructure of the fabricated layer, as mentioned in the previous section. As depicted in Fig. 8, the maximum hardness in the range of 20–25 GPa are observed in the “flat” regions, whereas the values in the range of 10–15 GPa are observed in the “serrated” areas. This could be associated with both the microstructure of these regions and their crystal orientation. In general, the hardness of the material may vary depending on its crystal orientation [57]. In the case of BCC alloys, considering the low-indexed planes, the highest hardness is

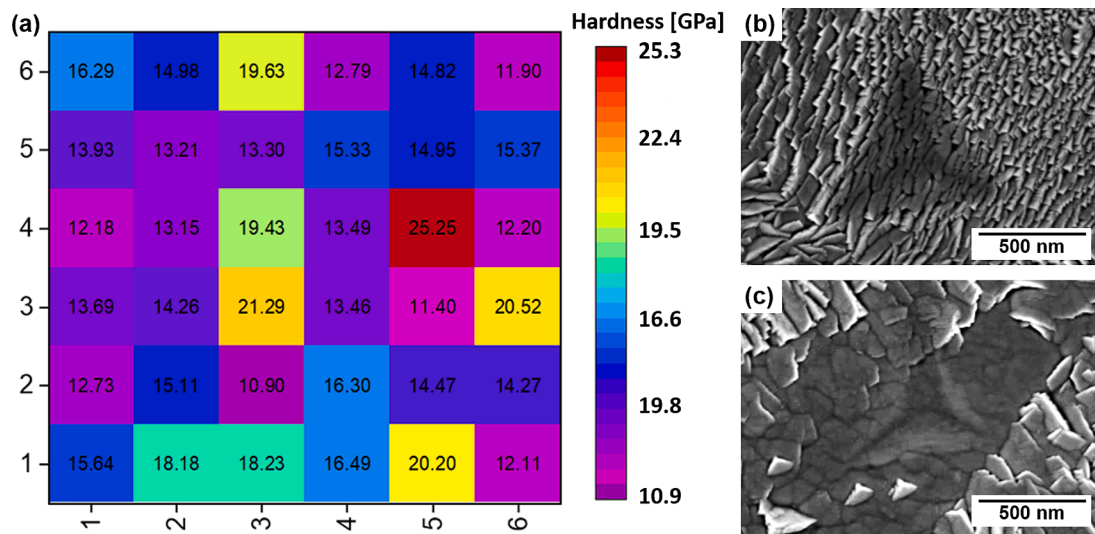


Fig. 8. Hardness map (a) and SEM images taken from the area of nanoindentation: column 1, row 1 (b) and column 5, row 4 (c).

typically observed for the $\{1\bar{1}0\}$ and $\{1\bar{1}\bar{1}\}$ -oriented grains, whereas the lowest for $\{0\bar{0}1\}$ -indexed ones [58,59]. This is especially visible for spherical nanoindentation, e.g. Beake et al. [60] reported a hardness of 3.87 GPa for $W_{(100)}$ and 4.79 GPa for $W_{(111)}$ in pure W. However, the differences are significantly lower if the Berkovich tip is used [61]. In the case of the W-Ta-Cr-V HEA, the highest hardness values above 20 GPa are observed in “flat” domains that exhibit orientations close to $\{0\bar{0}1\}$ relative to the surface. This indicates that the lower hardness of “serrated” regions is not related to their orientation but originate from their microstructure. The columns, in the case of “serrated” areas, are oriented parallel to the direction of the force during the nanoindentation test. This could result in the formation of crack at the boundaries of columns, which decreases the hardness compared to the “flat” areas where the columns do not exist.

He^+ ion irradiation behavior

Fig. 9a and Fig. 10a show the TEM micrographs of W-Ta-Cr-V HEA irradiated using He^+ ions up to fluences of $1 \times 10^{16} \text{ cm}^{-2}$ (LF) and $5 \times 10^{16} \text{ cm}^{-2}$ (HF), respectively. The images were acquired in the under-focus conditions to reveal the occurrence of the He bubbles that appear as bright spots under this condition. The corresponding He concentration profiles, calculated using SRIM software, were superimposed on the micrographs. The TEM observations performed along the cross-section of the samples are consistent with the implant profiles calculated using SRIM software, since the maximum density of the bubbles was found at a depth of about 500 nm. The magnified images of those areas are presented in Fig. 9b-d and Fig. 10b-d for LF and HF samples, respectively. In both cases, the investigations reveal the presence of fine He bubbles, with a size below 1 nm. Although there is a five-fold increase of the He concentration in the peak region between the LF and HF sample, the size of the bubbles remains almost unchanged – the

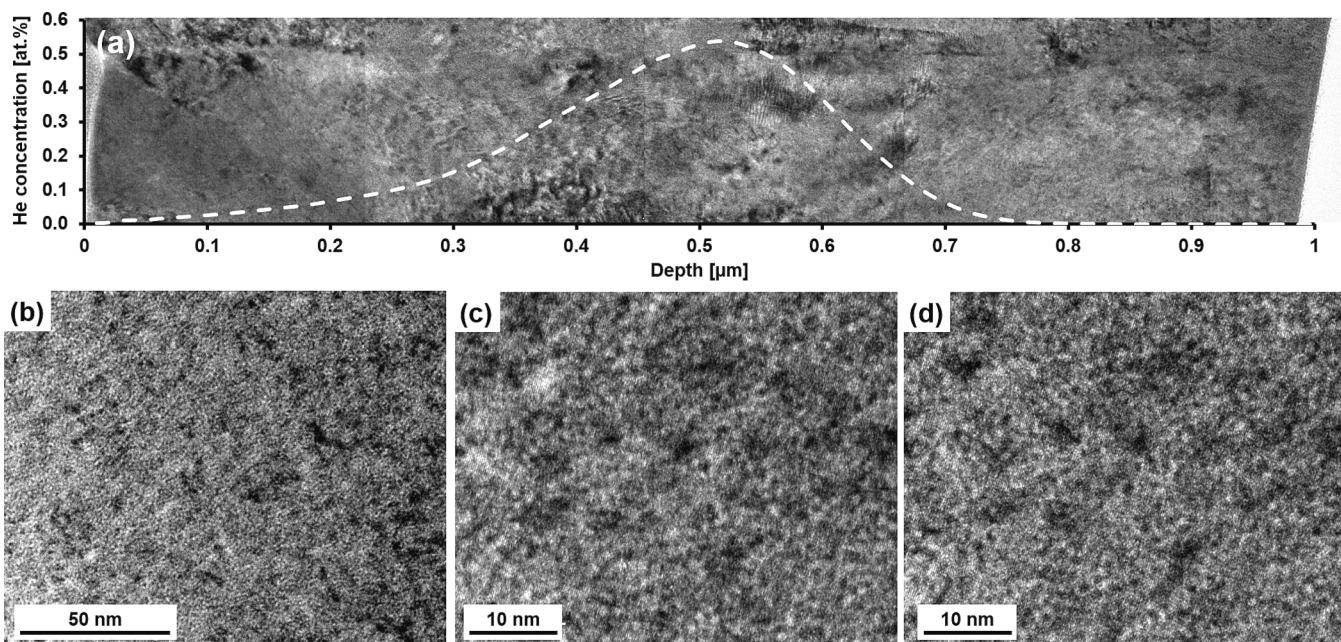


Fig. 9. TEM microstructure (under-focus) of the LF-W-Ta-Cr-V sample with superimposed He concentration distribution calculated by SRIM software (a) and micrographs taken from area of highest He concentration: low-magnification under-focus (b) and high-magnification under-focus (c), and over-focus (d).

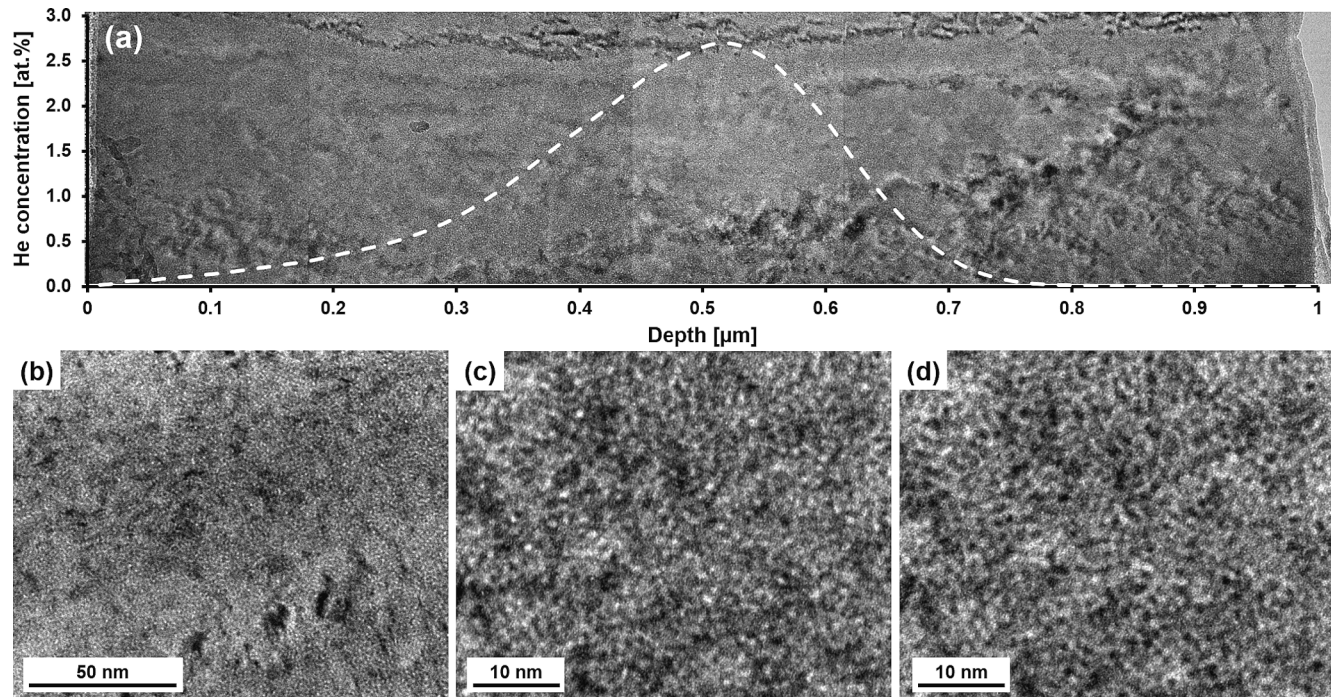


Fig. 10. TEM microstructure (under-focus) of the HF-W-Ta-Cr-V sample with a superimposed He concentration distribution calculated by SRIM software (a) and micrographs taken from the area of the highest He concentration: low-magnification under-focus (b) and high-magnification under-focus (c), and over-focus (d).

average size of the bubbles increased from 0.5 nm (LF sample) to about 0.6 nm (HF sample). Taking this into account, it can be concluded that with the increasing fluence of He the density of the bubbles in the microstructure of the material increase. This statement seems to be true also considering the differences in the microstructure of the investigated samples (e.g., Fig. 9d and Fig. 10d). Unfortunately, taking into consideration the size of the bubbles (<1 nm) and the thickness of the investigated thin foils (40—60 nm), a reliable estimation of their density is impossible due to, among others, an overlapping of bubbles. Because of that, we calculated the areal density of the detectable bubbles (with a size above ~ 0.2 nm) in five 50×50 nm 2 areas in the peak region (from 450 nm to 550 nm below the surface). The measurements were conducted on images acquired under the same imaging conditions from samples of similar thickness (~ 45 nm; measured using ELLS method) to minimize the factors that could influence the findings. The obtained results indicate that the density of the He bubbles increases from 1.1×10^{13} cm $^{-2}$ (LF) to 2.1×10^{13} cm $^{-2}$ (HF) with the increasing fluence of He $^{+}$ -ions, as shown in Table 2. Although those values are not equivalent to the density of bubbles, it gives a general view of the He bubbles formation process in the investigated material. What is important, in both cases the bubbles are uniformly distributed in the matrix, with no preferential nucleation sites at grain boundaries, and do not form any bigger agglomerates even at the higher fluence.

To investigate the potential occurrence of chemical segregation and/or the formation of secondary phases during the irradiation, a series of TEM investigations were conducted on the sample irradiated with a higher fluence of He. The study focused on two distinct regions within the material: firstly, the area characterized by the highest He concentration resulting from the irradiation, and secondly, the bottom part of the layer, as depicted in Fig. 11. This lower segment served as a

reference point since it remained unexposed to the irradiation and can be considered as pristine state. Significantly, both SAED patterns marked as D1 and D2, derived from the irradiated and pristine zones respectively, reveal the presence of the BCC solid solution phase. Notably, no additional spots corresponding to secondary phases were detected within the irradiated zone. The EDS elemental maps for those areas (M1 and M2) indicate no chemical segregation, and within both regions, all the elements were uniformly distributed within the matrix. All of this indicates the high structural stability of the investigated material under He $^{+}$ -ion irradiation. Although the irradiation process led to the formation of fine He bubbles (Fig. 10), it did not induce phase transformations or the segregation of constituent elements. This outcome is essential from the point of view of the irradiation resistance of this material.

Helium is generated in structural materials of fusion reactors through transmutation reactions emitting α particles and via implanted helium produced via fusion in the plasma. It is practically insoluble in metals, and hence it tends to precipitate in the form of bubbles, which may result in the embrittlement of materials [54]. Considering this, understanding the behavior of the He bubbles formation is essential from the point of view of the application of any new material in the nuclear industry, especially in the case of plasma-facing components. It is broadly accepted that the He $^{+}$ ion irradiation may be applied to simulate the effects of α -particle generation in transmutation reactions. Because of that, we used this technique to study He bubble formation behavior in the new equimolar W-Ta-Cr-V HEA. The formation mechanism of the bubbles is closely connected to the occurrence of vacancies in the structure of the materials formed by knock-out damage. At low irradiation temperatures, the low thermal mobility of the vacancies limits voids growth [6]. Typically, the He $^{+}$ irradiation at temperatures close to room temperature (RT) leads to the formation of fine He bubbles in the microstructure of various structural materials. For example, Yu et al. [62] reported the presence of ~ 1 nm bubbles in nanocrystalline Fe irradiated with 100 keV He $^{+}$ ions at RT (fluence 6×10^{16} cm $^{-2}$). Similarly, the nanometric He bubbles were registered in He $^{+}$ irradiated W and W-based alloys [6,63]. Shen et al. [64] stated that for pure W, no bubbles could be observed by TEM for fluences lower than 1×10^{15} cm $^{-2}$. In the case of W-Ta-Cr-V HEA investigated here, bubbles were

Table 2

The size and density of He bubbles in relation to the applied He $^{+}$ -ion fluence.

He fluence	He bubbles areal density	Average He bubbles size
1×10^{16} cm $^{-2}$ (LF)	$1.1 (\pm 0.1) \times 10^{13}$ cm $^{-2}$	0.5 ± 0.1 nm
5×10^{16} cm $^{-2}$ (HF)	$2.1 (\pm 0.2) \times 10^{13}$ cm $^{-2}$	0.6 ± 0.2 nm

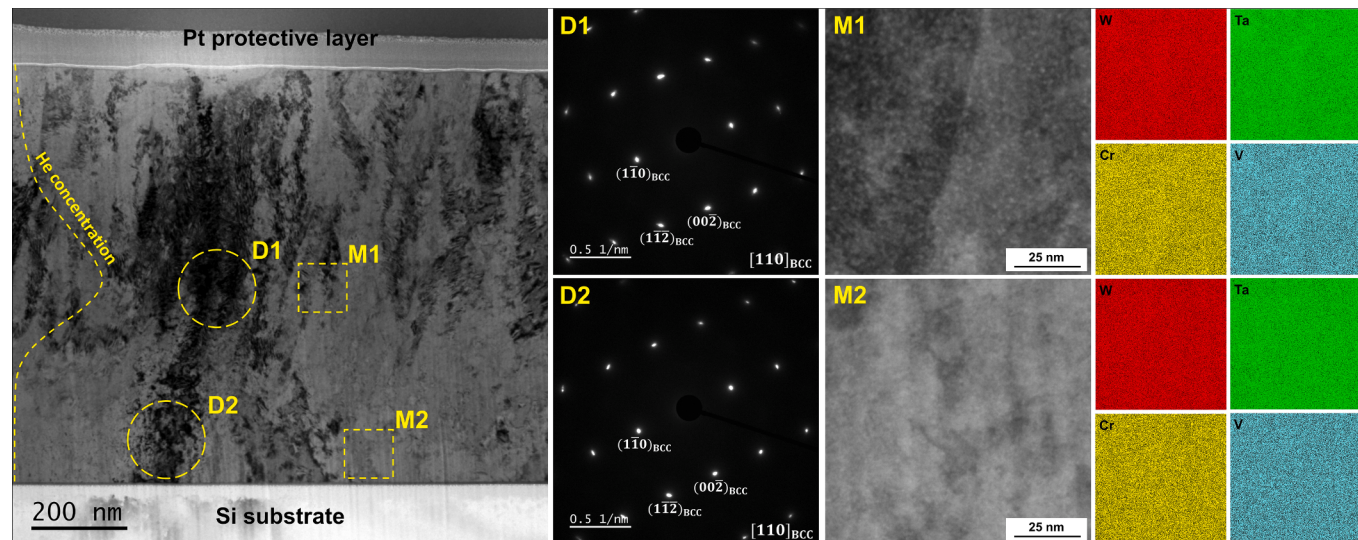


Fig. 11. TEM/BF micrograph of the HF-W-Ta-Cr-V sample with the superimposed He concentration distribution and corresponding SAED patterns (D1 and D2) and EDS elemental maps (M1 and M2).

observed at both applied He^+ fluences – $1 \times 10^{16} \text{ cm}^{-2}$ and $5 \times 10^{16} \text{ cm}^{-2}$. With the increase of the He^+ fluence, the density of bubbles increase, whereas their average size remains almost unchanged. This means that the He damage proceeded by the nucleation of new bubbles and not by their growth, which is related to the low He mobility at RT in the structure of the investigated HEA. However, the size of the bubbles in the studied W-Ta-Cr-V alloy was slightly smaller in comparison to those previously observed in pure W irradiated at RT with similar fluences [6,63,65]. Similarly, their size was reduced in comparison to the previously investigated FCC-HEAs such as CoCrFeNi (1.3–2.1 nm) [66] or BCC-HEAs e.g. Al_{1.5}CoCrFeNi (2.5 nm) [56]. The bubbles in the analyzed area were uniform and randomly distributed in the matrix, which indicates their homogenous nucleation and growth during the irradiation. It is important to note that the TEM observations did not reveal any evidence of the preferential bubble formation on grain boundaries, which is essential from the point of view of the irradiation resistance of this material. As shown in Ref. [55], the presence of large bubbles located on the grain boundaries (or their proximity) typically results in the degradation of the performance of the structural materials – embrittlement, ductility deterioration, creep, and fatigue life reduction.

It is well-known that during the ion irradiation the interactions of incident particles with the atoms in the crystal structure of the material lead among others to the formation of the Frenkel pairs [67]. Although vacancies are preferentially bonded with He atoms in He-vacancy complexes, the excess interstitials contribute to the formation of dislocation loops [54]. The dislocation loops may also be generated, especially at low temperatures, by a loop punching mechanism. In this process, an over-pressurized He bubble may enlarge by punching the matrix atoms into interstitial sites, thereby emitting a prismatic dislocation loop [68]. Although the occurrence of dislocation loops after ion irradiation is typical for a variety of metals, even at low dpa [69,70], in the case of the investigated W-Ta-Cr-V, no dislocation loops were registered during the TEM observations. Pure W is prone to loop formation; their occurrence is observed in self-ion irradiated W even at damage levels as low as 0.01 dpa [29,71]. Similarly, large dislocation loops are observed at damage levels not exceeding 1 dpa in other materials, such as W-TiC nanocomposites [72], Fe [73], and stainless steel [74]. The occurrence of interstitial dislocation loops is also observed in light-ion irradiated pure W. Zhao et al. [75] have reported the formation of dislocation loops below 0.1 dpa in W irradiated with 80 keV He^+ ions at RT. Recently, it has been shown that the W-based HEAs exhibited

superior resistance to loops formation under heavy ion irradiation [23]. In this case, no dislocation loops have been observed in the microstructure of W38-Ta36-Cr15-V11 HEA irradiated with 1 MeV Kr^{2+} ions up to 8 dpa at RT and 1073 K. The explanation of this phenomenon may be connected with the probability of the defect's recombination – due to similar defects mobilities in the investigated HEA, the probability of their recombination is high [23,76]. On the other hand, interstitial mobility in W is much higher compared to vacancies, and therefore, W-vacancy recombination rate is significantly lower [27]. This is in good agreement with the results of Byggmästar et al. [27] for BCC-structured Mo-Nb-Ta-V-W HEA. Using a machine-learned interatomic potential they found that in contrast to W, the interstitials in the HEA form fine loops enriched in V, which may be experimentally invisible.

Unfortunately, there is no literature on the RT-irradiation behavior of W-Ta-Cr-V-based HEA under light ions bombardment. Recently, El-Atwani et al. [30] investigated the performance of W35-Ta35-V15-Cr15 HEA under low energy He^+ irradiation at temperature of 1223 K. In this case, the formation of fine (2–3 nm) He bubbles uniformly distributed in the matrix were observed. Despite the higher irradiation temperature and thus the increased mobility of He in the structure of HEA in comparison to the studied case, no favorable bubble formation on the grain boundaries was observed. This confirms the superior He irradiation resistance of the W-Ta-Cr-V-based HEAs compared to the nanocrystalline W or W-TiC composites for which efficient He trapping at the grain boundaries was previously reported [72]. This phenomenon could be associated with the presence of sites with low formation energy that can act as strong traps for He in the structure of HEA, limiting its migration. Since the migration barrier in W-based HEA is significantly higher in comparison to the pure W, it seems that He atoms tend to find a fairly stable site that can become bubble nuclei, which enhances the nucleation of fine bubbles [30]. Considering other investigated HEAs, they generally demonstrate high resistance to He^+ irradiation when compared with pure elements or conventional alloys, e.g., Yang et al. [77] reported high structural stability against He irradiation of FCC-structured Cr-Mn-Fe-Co-Ni HEA in comparison to pure Ni and 304 stainless steel. This is most likely associated with the complex defects energy landscape in HEAs that affects defect kinetics [8]. Precisely, the mobility of interstitials in HEAs is essentially decreased, whereas the mobility of vacancies is increased. This reduces the mobility gap between the Frenkel pairs and favors the recombination of defects [24,78]. Modeling efforts on chemically complex alloys have revealed wider distributions of defect energetics, and overlapping distributions of

formation and migration energies could potentially result in the improved recombination of interstitials and vacancies [79,80,81]. Moreover, sluggish diffusion and inefficient radiation heat conduction may also further enhance defect recombination [8,80]. As a result, fewer vacancies are available for the growth of the bubbles. Furthermore, the chemically complex environment around each atom reduces He diffusion and helps to trap He in small clusters [24,82]. Wang et al. [32] reported that the increasing chemical complexity of alloys helps suppress bubble formation in HEA; however, certain alloying elements (e.g., Fe) demonstrate higher efficiency in suppressing bubble growth than their counterparts (e.g., Cr and Mn).

The presented results indicate the high irradiation resistance of the newly developed equimolar W-Ta-Cr-V RHEA against He-induced defect formation. Although He^+ -ion irradiation led to the formation of the fine He bubbles within its microstructure, their size was smaller in comparison to those observed in pure W, previously investigated HEAs, and conventional materials used in the nuclear industry that were irradiated with He^+ -ions at room temperature. Importantly, the He^+ -irradiation did not result in the extensive irradiation-hardening or the formation of any other defects except for the mentioned He bubbles. Taking all of this into account, the developed W-Ta-Cr-V RHEA appears to be a valuable candidate for future studies, potentially serving as a replacement for tungsten in critical structural components of forthcoming fusion reactors, such as plasma-facing components. However, to assess the performance of this material in PFM operating conditions, the evolution of He bubbles at elevated temperatures must be investigated in more details, which will be a subject of our future works.

Summary

In the present work, the microstructure, mechanical properties, and He^+ irradiation resistance of new equimolar W-Ta-Cr-V HEA were systematically investigated. The material was fabricated in the form of a 1 μm thick layer deposited on a Si substrate using a magnetron sputtering method. It formed a single-phase BCC solid solution, without any sign of segregation or occurrence of secondary phases. The microstructure of the alloy consisted of micrometric domains that exhibited internal structure controlled by their crystal orientation relative to the surface. Results from complementary characterization techniques show that the {111} and {011}-oriented domains contain similarly oriented nanocolumns elongated into the layer growth direction, whereas {001}-oriented ones were monocrystalline. The average nanohardness of W-Ta-Cr-V alloy of 13 ± 2 GPa significantly exceeds the hardness of nanocrystalline pure W. This resulted from a high solid-solution strengthening effect induced by considerable differences in the atomic radius of elements randomly distributed in the crystal structure of the alloy.

In order to establish the irradiation resistance of the W-Ta-Cr-V HEA, the alloy was irradiated with 200 keV He^+ ions at room temperature. We found that this resulted in the formation of a high density of extremely fine He bubbles that were uniformly distributed in the matrix. With the increase of He^+ fluence from $1 \times 10^{16} \text{ cm}^{-2}$ to $5 \times 10^{16} \text{ cm}^{-2}$, the size of the bubbles remains almost unchanged, which taking into account the increased number of introduced He atoms, most probably leads to the increase of the bubbles density. This demonstrates that He accumulation proceeds by the nucleation of new He bubbles, rather than by their growth in size. This could be associated with enhanced defect recombination or reduced mobility of He in multicomponent alloys, in comparison to the pure W, as reported previously in the literature. The results obtained within the scope of this work indicate the promising irradiation resistance of the new equimolar W-Ta-Cr-V HEA, considering the presence of fine, uniformly distributed He-bubbles, the absence of dislocation loops, and negligible irradiation hardening. This makes this material a valuable candidate for further study as a replacement of tungsten in key structural components in future fusion reactors, such as plasma-facing materials.

CRediT authorship contribution statement

D. Kalita: Conceptualization, Methodology, Investigation, Writing – original draft, Writing – review & editing, Visualization, Validation. **I. Józwik:** Conceptualization, Supervision, Writing – review & editing. **L. Kurpaska:** Resources, Supervision, Writing – review & editing. **Y. Zhang:** Conceptualization, Resources, Supervision, Writing – review & editing. **K. Mulewska:** Investigation, Writing – review & editing. **W. Chrominski:** Investigation, Writing – review & editing. **J. O'Connell:** Investigation, Writing – review & editing. **Y. Ge:** Investigation, Writing – review & editing. **W.L. Boldman:** Resources, Writing – review & editing. **P.D. Rack:** Resources, Writing – review & editing. **Y. Wang:** Resources, Writing – review & editing. **W.J. Weber:** Conceptualization, Writing – review & editing. **J. Jagielski:** Conceptualization, Project administration, Writing – review & editing.

Declaration of Competing Interest

The authors declare that they have no known competing financial interests or personal relationships that could have appeared to influence the work reported in this paper.

Data availability

Data will be made available on request.

Acknowledgement

This publication is part of a project that has received funding from the European Union's Horizon 2020 research and innovation programme under grant agreement No 857470 and from the European Regional Development Fund via the Foundation for Polish Science International Research Agenda PLUS program grant No. MAB PLUS/2018/8 and South African National Research Foundation (118681). This work has been partially supported by the INLAS project financed by the Polish National Centre for Research and Development (PL-RPA2/01/INLAS/2019). YZ is supported through the Laboratory Directed Research and Development Program at Idaho National Laboratory under the Department of Energy (DOE) Idaho Operations Office (an agency of the U.S. Government) Contract DE-AC07-05ID145142. This work was performed, in part, at the Center for Integrated Nanotechnologies, an Office of Science User Facility operated for the U.S. Department of Energy (DOE) Office of Science. Los Alamos National Laboratory, an affirmative action equal opportunity employer, is managed by Triad National Security, LLC for the U.S. Department of Energy's NNSA, under contract 89233218CNA000001.

References

- [1] M.J. Baldwin, R.P. Doerner, Helium induced nanoscopic morphology on tungsten under fusion relevant plasma conditions, Nucl. Fusion 48 (2008) 5, <https://doi.org/10.1088/0029-5515/48/3/035001>.
- [2] Y. Ueda, et al., Research status and issues of tungsten plasma facing materials for ITER and beyond, Fusion Eng. Des. 89 (7–8) (2014) 901–906, <https://doi.org/10.1016/J.FUSENGDES.2014.02.078>.
- [3] D. Nishijima, M.Y. Ye, N. Ohno, S. Takamura, Incident ion energy dependence of bubble formation on tungsten surface with low energy and high flux helium plasma irradiation, J. Nucl. Mater. 313–316 (Mar. 2003) 97–101, [https://doi.org/10.1016/S0022-3115\(02\)01368-5](https://doi.org/10.1016/S0022-3115(02)01368-5).
- [4] V. Philippss, Tungsten as material for plasma-facing components in fusion devices, J. Nucl. Mater. 415 (1) (Aug. 2011) S2–S9, <https://doi.org/10.1016/J.JNUCMAT.2011.01.110>.
- [5] J.A.R. Wright, A review of late-stage tungsten fuzz growth, Tungsten 4 (Sep. 2022) 184–193, <https://doi.org/10.1007/s42864-021-00133-2>.
- [6] H. Iwakiri, K. Yasunaga, K. Morishita, N. Yoshida, Microstructure evolution in tungsten during low-energy helium ion irradiation, J. Nucl. Mater. 283–287 (2000) 1134–1138, [https://doi.org/10.1016/S0022-3115\(00\)00289-0](https://doi.org/10.1016/S0022-3115(00)00289-0).
- [7] B. Cantor, I.T.H. Chang, P. Knight, A.J.B. Vincent, Microstructural development in equiatomic multicomponent alloys, Mater. Sci. Eng. A 375–377 (Jul. 2004) 213–218, <https://doi.org/10.1016/J.MSEA.2003.10.257>.

- [8] Y. Zhang, Y.N. Osetsky, W.J. Weber, Tunable Chemical Disorder in Concentrated Alloys: Defect Physics and Radiation Performance, *Chem. Rev.* 122 (1) (2022) 789–829, <https://doi.org/10.1021/acs.chemrev.1c00387>.
- [9] D.B. Miracle, High-Entropy Alloys: A Current Evaluation of Founding Ideas and Core Effects and Exploring ‘Nonlinear Alloys’, *JOM* 69 (11) (2017) 2130–2136, <https://doi.org/10.1007/s11837-017-2527-z>.
- [10] Y. Zhang, W.J. Weber, Ion irradiation and modification: The role of coupled electronic and nuclear energy dissipation and subsequent nonequilibrium processes in materials, *Appl. Phys. Rev.* 7 (4) (2020), <https://doi.org/10.1063/5.0027462>.
- [11] W. Li, D. Xie, D. Li, Y. Zhang, Y. Gao, P.K. Liaw, Mechanical behavior of high-entropy alloys, *Prog. Mater. Sci.* 118 (May 2021), 100777, <https://doi.org/10.1016/J.PMATSCL.2021.100777>.
- [12] E.P. George, W.A. Curtin, C.C. Tasan, High entropy alloys: A focused review of mechanical properties and deformation mechanisms, *Acta Mater.* 188 (Apr. 2020) 435–474, <https://doi.org/10.1016/J.ACTAMAT.2019.12.015>.
- [13] O.N. Senkov, G.B. Wilks, D.B. Miracle, C.P. Chuang, P.K. Liaw, Refractory high-entropy alloys, *Intermetallics* 18 (9) (Sep. 2010) 1758–1765, <https://doi.org/10.1016/J.IINTERMET.2010.05.014>.
- [14] O.N. Senkov, G.B. Wilks, J.M. Scott, D.B. Miracle, Mechanical properties of Nb₂₅Mo₂₅Ta₂₅W₂₅ and V₂₀Nb₂₀Mo₂₀Ta₂₀W₂₀ refractory high entropy alloys, *Intermetallics* 19 (5) (May 2011) 698–706, <https://doi.org/10.1016/J.IINTERMET.2011.01.004>.
- [15] X. Wang, H. Huang, J. Shi, H.-Y. Xu, D.-Q. Meng, Recent progress of tungsten-based high-entropy alloys in nuclear fusion, *Tungsten* 3 (2021) 143–160, <https://doi.org/10.1007/s42864-021-00092-8>.
- [16] S. Xia, M.C. Gao, T. Yang, P.K. Liaw, Y. Zhang, Phase stability and microstructures of high entropy alloys ion irradiated to high doses, *J. Nucl. Mater.* 480 (Nov. 2016) 100–108, <https://doi.org/10.1016/J.JNUCMAT.2016.08.017>.
- [17] S. Abhaya, R. Rajaraman, S. Kalavathi, C. David, B.K. Panigrahi, G. Amarendra, Effect of dose and post irradiation annealing in Ni implanted high entropy alloy FeCrCoNi using slow positron beam, *J. Alloy. Compd.* 669 (Jun. 2016) 117–122, <https://doi.org/10.1016/J.JALLCOM.2016.01.242>.
- [18] T. Nagase, P.D. Rack, J.H. Noh, T. Egami, In-situ TEM observation of structural changes in nano-crystalline CoCrCuFeNi multicomponent high-entropy alloy (HEA) under fast electron irradiation by high voltage electron microscopy (HVEM), *Intermetallics* 59 (2015) 32–42, <https://doi.org/10.1016/J.IINTERMET.2014.12.007>.
- [19] Z. Cheng, et al., Irradiation effects in high-entropy alloys and their applications, *J. Alloy. Compd.* 930 (Jan. 2023), <https://doi.org/10.1016/J.JALLCOM.2022.166768>.
- [20] M.R. Gilbert, et al., Waste implications from minor impurities in European DEMO materials, *Nucl. Fusion* 59 (2019) 7, <https://doi.org/10.1088/1741-4326/ab154e>.
- [21] M. Sadeghilardjani, et al., Ion irradiation response and mechanical behavior of reduced activity high entropy alloy, *J. Nucl. Mater.* 529 (Feb. 2020), <https://doi.org/10.1016/J.JNUCMAT.2019.151955>.
- [22] S. Chang, K.K. Tseng, T.Y. Yang, D.S. Chao, J.W. Yeh, J.H. Liang, Irradiation-induced swelling and hardening in HfNbTaTiZr refractory high-entropy alloy, *Mater. Lett.* 272 (Aug. 2020), <https://doi.org/10.1016/J.MATLET.2020.127832>.
- [23] O. El-Atwani, et al., Outstanding radiation resistance of tungsten-based high-entropy alloys, *Sci. Adv.* 5 (3) (2019), <https://doi.org/10.1126/SCIADEVAAV2002>.
- [24] Y. Zhang, et al., Effects of 3d electron configurations on helium bubble formation and void swelling in concentrated solid-solution alloys, *Acta Mater.* 181 (2019) 519–529, <https://doi.org/10.1016/j.actamat.2019.10.013>.
- [25] C. Lu, et al., Enhancing radiation tolerance by controlling defect mobility and migration pathways in multicomponent single-phase alloys, *Nat. Commun.* 7 (2016) 1–8, <https://doi.org/10.1038/ncomms13564>.
- [26] A. Barashev, Y. Osetsky, H. Bei, C. Lu, L. Wang, Y. Zhang, Chemically-biased diffusion and segregation impede void growth in irradiated Ni-Fe alloys, *Curr. Opin. Solid State Mater. Sci.* 23 (2) (2019) 92–100, <https://doi.org/10.1016/j.cosss.2018.12.001>.
- [27] J. Byggmästar, K. Nordlund, F. Djurabekova, Modeling refractory high-entropy alloys with efficient machine-learned interatomic potentials: Defects and segregation, *Phys. Rev. B* 104 (10) (2021) 1–11, <https://doi.org/10.1103/PhysRevB.104.104101>.
- [28] X. Hu, et al., Irradiation hardening of pure tungsten exposed to neutron irradiation, *J. Nucl. Mater.* 480 (Nov. 2016) 235–243, <https://doi.org/10.1016/J.JNUCMAT.2016.08.024>.
- [29] W. Chrominski, L. Ciupinski, P. Bazarnik, S. Markelj, T. Schwarz-Selinger, TEM investigation of the influence of dose rate on radiation damage and deuterium retention in tungsten, *Mater. Charact.* 154 (Aug. 2019) 1–6, <https://doi.org/10.1016/J.MATCHAR.2019.05.028>.
- [30] O. El-Atwani, et al., Helium implantation damage resistance in nanocrystalline W-Ta-V-C high entropy alloys, *Mater. Today Energy* 19 (Mar. 2021), <https://doi.org/10.1016/J.MTENER.2020.100599>.
- [31] H. Cui, N. Liu, L. Luo, Y. Xu, J. Cheng, Y. Wu, Behavior of high-entropy W-rich alloys W_x(TaVCrTi)_y under He⁺ irradiation, *Fusion Eng. Des.* vol. 172, no. July (2021), 112904, <https://doi.org/10.1016/j.fusengdes.2021.112904>.
- [32] X. Wang, et al., Understanding effects of chemical complexity on helium bubble formation in Ni-based concentrated solid solution alloys based on elemental segregation measurements, *J. Nucl. Mater.* 569 (2022), 153902, <https://doi.org/10.1016/j.jnucmat.2022.153902>.
- [33] Y. Zhang, et al., Role of electronic energy loss on defect production and interface stability: Comparison between ceramic materials and high-entropy alloys, *Curr. Opin. Solid State Mater. Sci.* 26 (4) (2022), 101001, <https://doi.org/10.1016/j.cosss.2022.101001>.
- [34] J.F. Ziegler, M.D. Ziegler, J.P. Biersack, SRIM – The stopping and range of ions in matter (2010), *Nucl. Instruments Methods Phys. Res. Sect. B Beam Interact. Mater. Atoms* 268 (2010) 1818–1823, <https://doi.org/10.1016/j.nimb.2010.02.091>.
- [35] W.J. Weber, Y. Zhang, Predicting damage production in monoatomic and multi-elemental targets using stopping and range of ions in matter code: Challenges and recommendations, *Curr. Opin. Solid State Mater. Sci.* 23 (4) (Aug. 2019), <https://doi.org/10.1016/J.COSSMS.2019.06.001>.
- [36] A.Y. Konobeyev, U. Fischer, Y.A. Korovin, S.P. Simakov, Evaluation of effective threshold displacement energies and other data required for the calculation of advanced atomic displacement cross-sections, *Nucl. Energy Technol.* 3 (3) (Sep. 2017) 169–175, <https://doi.org/10.1016/J.NUCET.2017.08.007>.
- [37] A.J. Schwartz, M. Kumar, B. L. Adams, D. P. Field, *EBSID in Materials Science*, Second Ed., vol. 86, no. 1. Springer, 2009. <https://doi.org/10.1016/j.actamat.2012>.
- [38] A.C. Fischer-Cripps, Critical review of analysis and interpretation of nanoindentation test data, *Surf. Coatings Technol.* 200 (14–15) (Apr. 2006) 4153–4165, <https://doi.org/10.1016/J.SURFCOAT.2005.03.018>.
- [39] W.C. Oliver, G.M. Pharr, An improved technique for determining hardness and elastic modulus using load and displacement sensing indentation experiments, *J. Mater. Res.* 7 (6) (1992) 1564–1583, <https://doi.org/10.1557/JMR.1992.1564>.
- [40] Y.S. Jung, D.W. Lee, D.Y. Jeon, Influence of dc magnetron sputtering parameters on surface morphology of indium tin oxide thin films, *Appl. Surf. Sci.* 221 (1–4) (Jan. 2004) 136–142, [https://doi.org/10.1016/S0169-4332\(03\)00862-6](https://doi.org/10.1016/S0169-4332(03)00862-6).
- [41] M. Kamei, Y. Shigesato, S. Takaki, Origin of characteristic grain-subgrain structure of tin-doped indium oxide films, *Thin Solid Films* 259 (1) (Apr. 1995) 38–45, [https://doi.org/10.1016/0040-6090\(94\)06390-7](https://doi.org/10.1016/0040-6090(94)06390-7).
- [42] E.P. George, D. Raabe, R.O. Ritchie, High-entropy alloys, *Nat. Rev. Mater.* 4 (8) (2019) 515–534, <https://doi.org/10.1038/s41578-019-0121-4>.
- [43] O.N. Senkov, J.M. Scott, S.V. Senkova, D.B. Miracle, C.F. Woodward, Microstructure and room temperature properties of a high-entropy TaNbHfZrTi alloy, *J. Alloy. Compd.* 509 (20) (May 2011) 6043–6048, <https://doi.org/10.1016/J.JALLCOM.2011.02.171>.
- [44] J.W. Yeh, et al., Nanostructured high-entropy alloys with multiple principal elements: Novel alloy design concepts and outcomes, *Adv. Eng. Mater.* 6 (5) (2004) 299–303, <https://doi.org/10.1002/ADEM.200300567>.
- [45] Z. Li, K.G. Pradeep, Y. Deng, D. Raabe, C.C. Tasan, Metastable high-entropy dual-phase alloys overcome the strength–ductility trade-off, *Nature* 534 (7606) (2016) 227–230, <https://doi.org/10.1038/nature17981>.
- [46] J. Jayaraj, P. Thirathipviwat, J. Han, A. Gebert, Microstructure, mechanical and thermal oxidation behavior of AlNbTiZr high entropy alloy, *Intermetallics* 100 (Sep. 2018) 9–19, <https://doi.org/10.1016/J.IINTERMET.2018.05.015>.
- [47] W.R. Wang, W.L. Wang, S.C. Wang, Y.C. Tsai, C.H. Lai, J.W. Yeh, Effects of Al addition on the microstructure and mechanical property of Al_xCoCrFeNi high-entropy alloys, *Intermetallics* 26 (Jul. 2012) 44–51, <https://doi.org/10.1016/J.IINTERMET.2012.03.005>.
- [48] Y. Shi, et al., Deuterium retention and desorption behavior of W-Ta-Cr-V high entropy alloy, *J. Nucl. Mater.* 568 (2022), 153897, <https://doi.org/10.1016/J.JNUCMAT.2022.153897>.
- [49] F.T.N. Vüller, R. Spolenak, Alpha- vs. beta-W nanocrystalline thin films: A comprehensive study of sputter parameters and resulting materials' properties, *Thin Solid Films* 577 (2015) 26–34, <https://doi.org/10.1016/j.tsf.2015.01.030>.
- [50] J.P. Singh, T. Karabacak, T.M. Lu, G.C. Wang, Nanoridge domains in α-phase W films, *Surf. Sci.* 538 (3) (Jul. 2003), [https://doi.org/10.1016/S0039-6028\(03\)00728-3](https://doi.org/10.1016/S0039-6028(03)00728-3).
- [51] Y.G. Shen, Y.W. Mai, Q.C. Zhang, D.R. McKenzie, W.D. McFall, W.E. McBride, Residual stress, microstructure, and structure of tungsten thin films deposited by magnetron sputtering, *J. Appl. Phys.* 87 (1) (2000) 177–187, <https://doi.org/10.1063/1.371841>.
- [52] O. El-Atwani, et al., Nanohardness measurements of heavy ion irradiated coarse- and nanocrystalline-grained tungsten at room and high temperature, *J. Nucl. Mater.* 509 (Oct. 2018) 276–284, <https://doi.org/10.1016/J.JNUCMAT.2018.06.023>.
- [53] Q. Wei, et al., Microstructure and mechanical properties of super-strong nanocrystalline tungsten processed by high-pressure torsion, *Acta Mater.* 54 (15) (Sep. 2006) 4079–4089, <https://doi.org/10.1016/J.ACTAMAT.2006.05.005>.
- [54] Y.-P. Li, et al., The influence of helium on the bulk properties of fusion reactor structural materials, *Nucl. Fusion* 24 (8) (Aug. 1984) 1039, <https://doi.org/10.1088/0029-5515/24/8/009>.
- [55] M. Cui, et al., He ion implantation induced He bubbles and hardness in tungsten, *Nucl. Mater. Energy* 15 (November 2017) (2018) 232–236, <https://doi.org/10.1016/j.nme.2018.05.004>.
- [56] G. Pu, et al., “Outstanding radiation tolerance and mechanical behavior in ultra-fine nanocrystalline Al 1.5 CoCrFeNi high entropy alloy films under He ion irradiation,” 2020, doi: 10.1016/j.apusc.2020.146129.
- [57] L. Kurpaska, M. Frelek-Kozak, K. Nowakowska-Langier, M. Lesniak, J. Jasinski, J. Jagielski, Structural and mechanical properties of Ar-ion irradiated YSZ single-crystals grown in different crystallographic orientations, *Nucl. Instruments Methods Phys. Res. Sect. B Beam Interact. Mater. Atoms* 409 (Oct. 2017) 81–85, <https://doi.org/10.1016/J.NIMB.2017.05.008>.
- [58] S. Pathak, D. Stojakovic, S.R. Kalidindi, Measurement of the local mechanical properties in polycrystalline samples using spherical nanoindentation and orientation imaging microscopy, *Acta Mater.* 57 (10) (Jun. 2009) 3020–3028, <https://doi.org/10.1016/J.ACTAMAT.2009.03.008>.
- [59] J.S. Weaver, et al., Quantifying the mechanical effects of He, W and He + W ion irradiation on tungsten with spherical nanoindentation, *J. Mater. Sci.* 53 (2018) 5296–5316, <https://doi.org/10.1007/s10853-017-1833-8>.

- [60] B.D. Beake, S. Goel, Incipient plasticity in tungsten during nanoindentation: Dependence on surface roughness, probe radius and crystal orientation, Int. J. Refract Metal Hard Mater. 75 (April) (2018) 63–69, <https://doi.org/10.1016/j.ijrmhm.2018.03.020>.
- [61] S. Jakob, et al., Influence of crystal orientation and Berkovich tip rotation on the mechanical characterization of grain boundaries in molybdenum, Mater. Des. 182 (Nov. 2019), <https://doi.org/10.1016/J.MATDES.2019.107998>.
- [62] K.Y. Yu, et al., Radiation damage in helium ion irradiated nanocrystalline Fe, J. Nucl. Mater. 425 (1–3) (2012) 140–146, <https://doi.org/10.1016/j.jnucmat.2011.10.052>.
- [63] W.Q. Chen, et al., Characterization of dose dependent mechanical properties in helium implanted tungsten, J. Nucl. Mater. 509 (Oct. 2018) 260–266, <https://doi.org/10.1016/J.JNUCMAT.2018.07.004>.
- [64] Z. Shen, et al., Effects of sequential helium and hydrogen ion irradiation on the nucleation and evolution of bubbles in tungsten, Fusion Eng. Des. 115 (2017) 80–84, <https://doi.org/10.1016/j.fusengdes.2017.01.001>.
- [65] M. Miyamoto, et al., Systematic investigation of the formation behavior of helium bubbles in tungsten, J. Nucl. Mater. 463 (Aug. 2015) 333–336, <https://doi.org/10.1016/J.JNUCMAT.2014.10.098>.
- [66] R.W. Harrison, G. Greaves, H. Le, H. Bei, Y. Zhang, S.E. Donnelly, Chemical effects on He bubble superlattice formation in high entropy alloys, 2019, doi: 10.1016/j.cossms.2019.07.001.
- [67] L.K. Murty, I. Charit, An Introduction to Nuclear Materials: Fundamentals and Applications, 1st Edition, 978-3-527-41201-3, 2013.
- [68] Y. Minyou, Effects of Low Energy and High Flux Helium/Hydrogen Plasma Irradiation on Tungsten as Plasma Facing Material, Plasma Sci. Technol 7 (2005) 2828, doi: 10.1088/1009-0630/7/3/010.
- [69] K. Mulewska et al., Self-ion irradiation of high purity iron: Unveiling plasticity mechanisms through nanoindentation experiments and large-scale atomistic simulations, 2023, doi: 10.1016/j.jnucmat.2023.154690.
- [70] M. Frelek-Kozak et al., Mechanical behavior of ion-irradiated ODS RAF steels strengthened with different types of refractory oxides, 2022, doi: 10.1016/j.apusc.2022.155465.
- [71] X. Yi, M.L. Jenkins, M.A. Kirk, Z. Zhou, S.G. Roberts, In-situ TEM studies of 150 keV W⁺ ion irradiated W and W-alloys: Damage production and microstructural evolution, Acta Mater. 112 (2016) 105–120, <https://doi.org/10.1016/j.actamat.2016.03.051>.
- [72] O. El Atwani, et al., In-Situ Helium Implantation and TEM Investigation of Radiation Tolerance to Helium Bubble Damage in Equiaxed Nanocrystalline Tungsten and Ultrafine Tungsten-TiC Alloy, Materials (Basel) 13 (3) (Feb. 2020) 794, <https://doi.org/10.3390/MA13030794>.
- [73] S.L. Dudarev, et al., Spatial ordering of nano-dislocation loops in ion-irradiated materials, J. Nucl. Mater. 455 (1–3) (Dec. 2014) 16–20, <https://doi.org/10.1016/J.JNUCMAT.2014.02.032>.
- [74] A. Etienne, M. Hernández-Mayoral, C. Genevois, B. Radiguet, P. Pareige, Dislocation loop evolution under ion irradiation in austenitic stainless steels, J. Nucl. Mater. 400 (1) (May 2010) 56–63, <https://doi.org/10.1016/J.JNUCMAT.2010.02.009>.
- [75] M. Zhao, et al., Fluence dependence of helium ion irradiation effects on the microstructure and mechanical properties of tungsten, Nucl. Instruments Methods Phys. Res. Sect. B Beam Interact. Mater. Atoms 414 (2018) 121–125, <https://doi.org/10.1016/j.nimb.2017.09.002>.
- [76] S. Zhao, Defect properties in a VTaCrW equiatomic high entropy alloy (HEA) with the body centered cubic (bcc) structure, J. Mater. Sci. Technol. 44 (2020) 133–139, <https://doi.org/10.1016/j.jmst.2019.10.025>.
- [77] L. Yang, et al., High He-ion irradiation resistance of CrMnFeCoNi high-entropy alloy revealed by comparison study with Ni and 304SS, J. Mater. Sci. Technol. 35 (2019) 300–305, <https://doi.org/10.1016/j.jmst.2018.09.050>.
- [78] D. Chen, et al., Diffusion controlled helium bubble formation resistance of FeCoNiCr high-entropy alloy in the half-melting temperature regime, J. Nucl. Mater. 526 (Dec. 2019), <https://doi.org/10.1016/J.JNUCMAT.2019.151747>.
- [79] S. Zhao, Y. Zhang, W.J. Weber, Engineering defect energy landscape of CoCrFeNi high-entropy alloys by the introduction of additional dopants, J. Nucl. Mater. 561 (153573) (2022), <https://doi.org/10.1016/J.JNUCMAT.2022.153573>.
- [80] S. Zhao, Y. Osetsky, Y. Zhang, Diffusion of point defects in ordered and disordered NiFe alloys, J. Alloy. Compd. 805 (2019) 1175–1183, <https://doi.org/10.1016/j.jallcom.2019.07.142>.
- [81] S. Zhao, Y. Osetsky, A.V. Barashev, Y. Zhang, Frenkel defect recombination in Ni and Ni-containing concentrated solid-solution alloys, Acta Mater. 173 (Jul. 2019) 184–194, <https://doi.org/10.1016/J.ACTAMAT.2019.04.060>.
- [82] S. Zhao, D. Chen, J.J. Kai, First-principles study of He behavior in a NiCoFeCr concentrated solid-solution alloy, Mater. Res. Lett. 7 (5) (May 2019) 188–193, <https://doi.org/10.1080/21663831.2019.1574926>.